Int J Adv Manuf Technol (2017) 89:3271–3284
DOI 10.1007/s00170-016-9249-1

ORIGINAL ARTICLE

Numerical investigation of the evolution of grit fracture and its impact on cutting performance in single grit grinding

Mei Yiming[1] · **Yu Zhonghua**[2] · **Yang Zhensheng**[3]

Received: 18 April 2016 / Accepted: 25 July 2016 / Published online: 18 August 2016

Abstract The study of single grit grinding with different geometries is important for understanding the micro-cutting behavior and material removal mechanism during grinding. However, the geometry of the grit changes during the wear process. The most fatal wear form responsible for the change in geometry is grit fracture as it causes considerable material loss instantaneously. This paper presents a new method to simulate single grit grinding with the fracture wear effects incorporated. The simulation procedure consists of three phases. The grinding force is calculated in phase 1, the grit fracture wear is simulated in phase 2, and the geometry of the grit after fracture wear is updated in phase 3. The evolution of grit fracture and its impact on cutting performance are studied by recycling the simulation procedure until the grit wears out. The results obtained reveal that the fracture wear is primarily caused by the maximum tensile stress along the rake surface or inside the grit. The resultant grinding force fluctuates during the chip formation process and is controlled by the number of cutting edges and the effective area of the flank surface. It decreases rapidly at the initial wear stage and varies with the dulling and self-sharpening action induced by the fracture wear. The volume of grinding chip decreases with an increase in the number of micro-cutting edges, which may result from a decrease in the ploughing effect.

Keywords Single grit grinding · Fracture wear · Finite element method · Grinding force · Grit geometry · Material removal

1 Introduction

With the increasing application of advanced materials, higher requirements for accuracy, efficiency, and cost have been raised in the field of mechanical manufacturing with respect to grinding. Grinding with tools, which makes use of special arrays of abrasive grits or regular micro-cutting edges aroused wide concern as it provides high grinding performance [1]. However, the effect of the grit geometrical parameters on the cutting behavior is still unknown, and limitations arise when dealing with the whole grinding wheel, primarily because of the stochastic distribution and orientation of the grits [2]. As the grinding process can be regarded as the summation of individual grit-workpiece interaction, numerous studies focusing on single grit grinding have been conducted to provide deep insight into the effects of the grit geometry on the material removal mechanism [3–6]. Tahsin and Chen conducted a single grit scratching test to analyze the effects of the grit shape on the material removal process, and found that material pile-up and the

✉ Yu Zhonghua
caq_221@zju.edu.cn

[1] The State Key Laboratory of Fluid Power Transmission and Control, College of Mechanical Engineering, Zhejiang University, Hangzhou 310027, Pepole's Republic of China

[2] Key Laboratory of Advanced Manufacturing Technology of Zhejiang Province, College of Mechanical Engineering, Zhejiang University, Hangzhou 310027, People's Republic of China

[3] School of Logistics Engineering, Shanghai Maritime University, Shanghai 201306, People's Republic of China

actual material removal area decrease with an increase in cutting depth [5]. Anderson et al. compared the cutting performance of spherical and truncated grits using the finite element method (FEM) [4]. The simulated results show that the grinding specific energy and grinding force of spherical grit is much bigger than that of the truncated grit, which suggests more sliding and ploughing energy is consumed in the dull grit. Axinte et al. investigated the impacts of the micro-cutting edges' geometry on the grinding process [2]. Three different shapes of grits (circular/square/triangular) were generated by laser ablation and mounted on a dummy grinding wheel. The material pile-up, elastic-plastic deformation and grinding force were compared using a scanning electron microscopy while machining brittle and ductile materials.

All of these studies have made significant contributions to single grit grinding research. However, the grits were found to wear by attrition, pull-out and grit fracture [7], and the grit geometry changes constantly during the wear process. Wu et al. suggested that mechanical wear of the grit induced by strains and stresses will result in deformation and fracture of the grit [8]. It was suggested by Shi and Malkin that grit fracture is the main wear form in the steady-state regime [9], and similar conclusions were drawn by Jackson, i.e., grit fracture plays an important role in changing the geometry of the grit, especially in large size grits [10]. Fujimoto and Ichida found that the fractal dimension of the cutting edges formed by grit fracture is higher than that formed by attrition wear, which suggests that grit fracture in the micro-cutting edges occupies a more important position with respect to controlling the geometry of the grit [11]. Severe geometrical changing of the grit was also found in the research by Ding et al. and they concluded that the grain remains sharp by means of fracture [12]. Therefore, grit fracture should be considered when investigating single grit grinding, as the cutting behavior as well as the interaction between the grit and workpiece is controlled by the geometry of the grit, which changes rapidly due to the instantaneous material loss caused by micro-fracture [13]. Numerous investigations of grit fracture based on experimental methods have been conducted to improve the grinding performance and extend the wheel life simultaneously. Scanning electron microscope was used to describe the geometry of the grit after fracture [11, 14], and other experimental methods such as Raman spectroscopy [15] and energy depressive X-ray [16] have also been used to make a deep insight into the stress distribution and film transition in the grit. However, limited by the small size and transient interactions of the grit, the experimental results are usually based on the average value of a measured volume of grits, which may cause inaccuracy in the resultant stress distribution [17]. Additionally, it is difficult to continuously observe the geometry of the grit during the wear process. Numerical methods such as the FEM have been used in prediction of grit fracture, as it has been proved to be efficient and accurate in simulation of chip formation and tool wear [18]. It is also effective for providing a time and spatially resolved calculations of the requisite physical results as an implementation of the experimental results [19]. Ding et al. studied the stress evolution of the grit results from grinding forces and brazing stress using a two-dimensional FE model [17], and they concluded that micro fracture is the predominant wear pattern of the grit, which is resulted from a dynamic grinding force [20]. Suh et al. found that the wear ratio is affected by the critical protrusion height of the grit

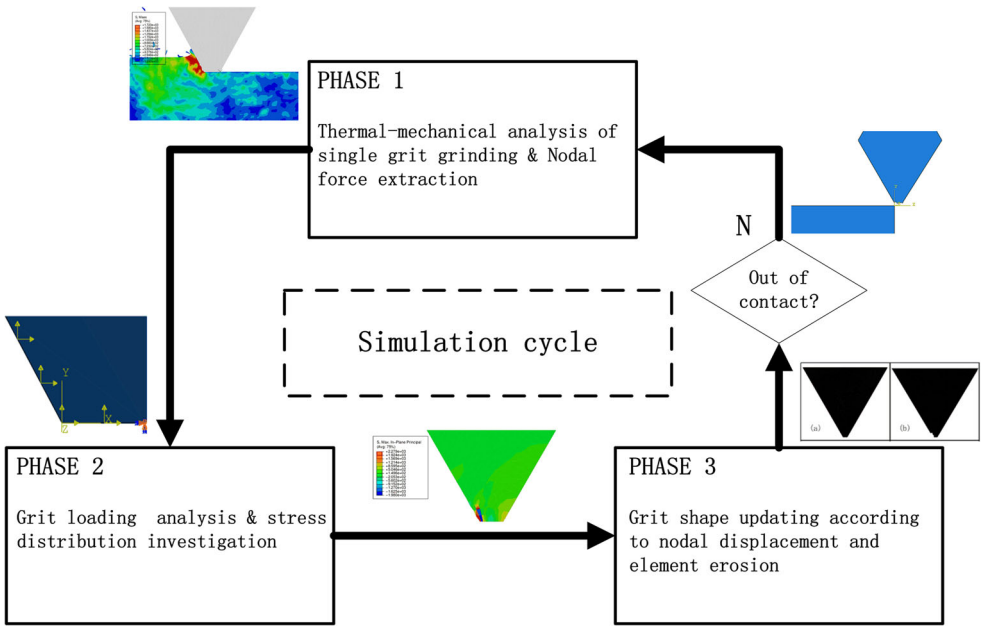

Fig. 1 Simulation procedure for single grit grinding incorporating grit fracture

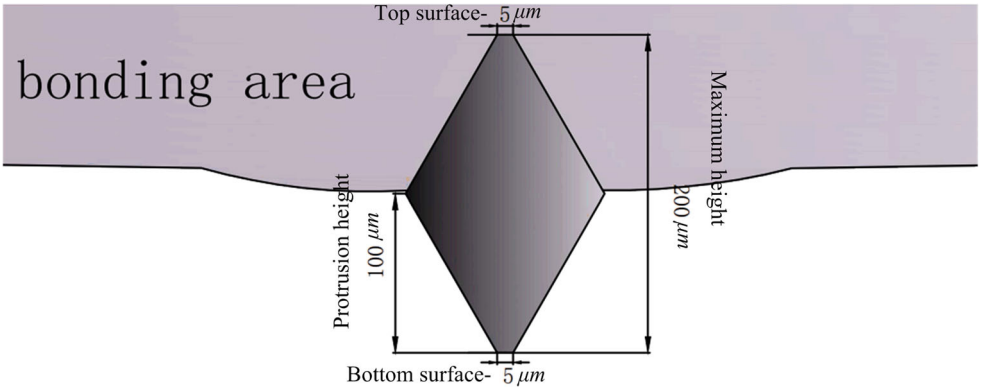

Fig. 2 Geometry of modeled grit

using a three-dimensional FE model [21]. It has also been found that the tensile stresses induced by the brazing and grinding is the main factor for bond and grit fracture. Akbari et al. used the Raman spectroscopy to analyze thermal residual stresses in brazed diamond metal joints: the stress field coupled with plasticity strain and the developed TiC interlayer were implemented through the FE model [22]. Jackson investigated the main wear form of the cubic born nitride (CBN) grit in brittle fracture FE mode. He concluded that grit fracture may be the dominant cause of material loss during grinding and that it is probably caused by mechanically induced tensile stress [10].

Considering the isolation of single grit grinding and grit fracture research, a single grit grinding model incorporating grit fracture based on FEM code Abaqus 6.14 is presented in this paper so as to elaborate the interrelationship between fracture and cutting performance. Attempts are made to illustrate the wear evolution of the grit geometry and its impact on cutting performance of the grit. The grinding force is calculated through single grit grinding simulation. The grit wear is studied through fracture analysis under the grinding forces, and the resultant stresses inside the grit are also obtained. The grit geometry is then updated according to the element erosion and node displacement. The impact of grit fracture on the cutting performance, such as the grinding force and material removal, are also studied by recycling the simulation procedure and comparing the results at various wear stages.

2 Finite element modeling of the single grit grinding incorporating grit fracture

2.1 Simulation procedure for single grit grinding incorporating grit fracture

The proposed procedure consists of three phases, as shown in Fig. 1. These phases form a simulation cycle and are repeated until the grit wears out. In phase 1, a single grit grinding model is created according to the predefined grinding parameters and grit geometry. The field outputs of grinding variables such as grinding force, stress and strain distributions are obtained. The grinding force along the rake surface of the grit is extracted in the form of an equivalent nodal force. In phase 2, a brittle cracking model is used to predict grit fracture and the variation of its geometry. The grinding force obtained in phase 1 is applied to the vertex of the grit along the contact area. The resultant stress distribution inside the grit during the grinding process is investigated. When loading is finished, the grit geometry is updated according to the deformation and material loss reflected by nodal displacement and element erosion in phase 3. Grids and boundaries are also refined to create a new geometrical model of the grit. The updated grit is then used in the next simulation cycle if the grit still maintains contact with the workpiece at a predefined cutting depth. The fractured grit geometry, grinding forces and material removal are compared between the results of each cycle to

Table 1 J-C plasticity model constants

Constant	AISI 4340
A(MPa)	710
B(MPa)	510
C	0.014
n	0.26
m	1.03
T_{tran}	293
T_{melt}	1793

Table 2 J-C dynamic failure model constants

Constant	AISI 4340
d_1	0.05
d_2	3.44
d_3	−2.12
d_4	0.002
d_5	0.61
T_{tran}	293
T_{melt}	1793

make a fundamental and visual comprehension of the grit wear evolution and its impact on the cutting performance.

2.2 Finite element model for single grit grinding

In this section, a single grit grinding FE model was created, and the grinding force and stress distribution were obtained. There are several existing FE models for single grit grinding and these models are sub-divided by some critical indexes in the work by Doman et al. [23]. The indexes used to divide model type suggests the critical procedures for creating a single grit grinding model: model dimension, grit geometry, material constitutive model for workpiece and grinding process settings. Considering that the simulation procedure will be recycled, a two dimensional model is chosen to reduce the computational cost in this paper.

CBN grit was chosen as the abrasive material because of its superior properties and wide utilization in the field of precision grinding. The geometry of CBN grit varies due to the complex manufacturing process, and there is a considerable discrepancy in the geometry between grit particles. In this paper, the initial grit geometry is assumed to be a rhombus with a very small plane on the top and bottom to represent the cross section of a newly plated grit, as has been illustrated by Jackson [10]. The maximum height of the grit is 200 μm corresponding to the standard 80/100 mesh size, the protrusion height of the grit is 100 μm, the rake angle of the grit is −30° and the width of its top and bottom surface is 5 μm, which is shown in Fig. 2. The grit and workpiece is meshed using 4-noded solid elements CPE4R(T) to conduct a mechanical-thermal coupled analysis and reduce the hourglassing.

The material of the workpiece is AISI 4340, and it is modeled with the Johnson-Cook plasticity model. This model is proposed by Johnson and Cook in 1983 [24] and it has been widely used in metal cutting simulation [3, 4, 25, 26]. Anderson et al. studied the process of abrasive-grain cutting: the Johnson-Cook plasticity model was chosen to model the material property of AISI 4340 [3, 4]. The comparison of numerical and experimental cutting forces under different cutting depth and cutting speed combinations proved that the Johnson-Cook plasticity model was accurate to describe the physics of abrasive-grain cutting.

Table 3 Conventional material properties

Property	CBN	AISI 4340
$\rho(kg/mm^3)$	3.4×10^{-6}	7.85×10^{-6}
E(GPa)	710	205
ν	0.15	0.29
K(W/(m.K))	80	44.5
C(J/(kg.K))	430	508

The effectiveness and feasibility of this constitutive model for AISI 4340 was also proven in the study of hard turning of AISI 4340 using variable micro-geometry PcBN tools. The simulated cutting forces were found to be in good agreements with the experimental results [26]. The Johnson-Cook plasticity model is an empirically derived Mises plasticity model in the analytical form of strain. The general form of this model is

$$\sigma = [A + B(\varepsilon_p)^n][1 + C(\ln \frac{\dot{\varepsilon_p}}{\dot{\varepsilon_0}})][1 - (\frac{T - T_{tran}}{T_{melt} - T_{tran}})^m] \quad (1)$$

where σ is the equivalent stress at nonzero strain rate, ε_p is the equivalent plastic strain, $\dot{\varepsilon_p}$ and $\dot{\varepsilon_0}$ are the equivalent plastic strain rate and reference strain rate, T_{tran} is the transient ambient temperature, T_{melt} is the melting temperature. The related strength parameters A, B, C, n and thermal parameters T_{tran}, T_{melt}, m for AISI4340 are summarized by Johnson and Cook [24], as illustrated in Table 1. To simulate chip formation in the grinding process, the Johnson-Cook dynamic failure model is used combined with the plasticity model. This dynamic failure model was proposed in 1985 [27] and validated by several researchers [25, 28]. Guo and Yen studied the mechanisms of discontinuous chip formation in high-speed machining of AISI 4340. They proved that the simulated chip morphology generally correlated well with the experimental data when the Johnson-Cook plasticity model and damage model were used together [25]. Similar conclusions were also obtained in the work by Zhang et al., where it was proved that the Johnson-Cook dynamic failure model is appropriate in simulating the cutting process of AISI 4340. The resultant cutting force and chip morphology matches well with the experiments within

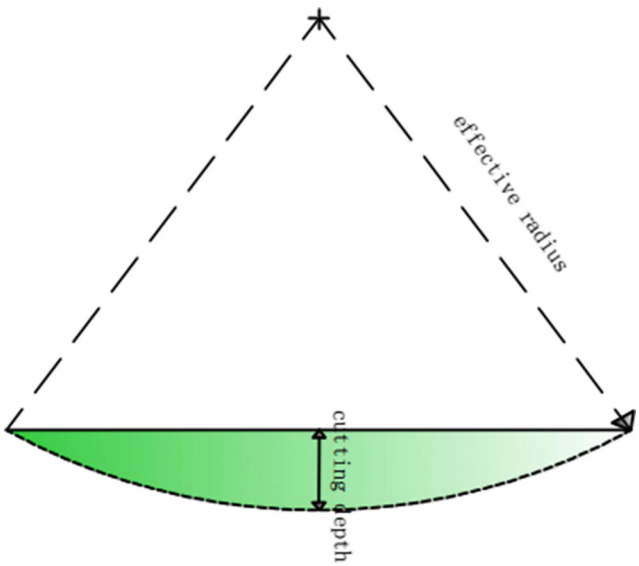

Fig. 3 Sketch map of the trajectory of the grit

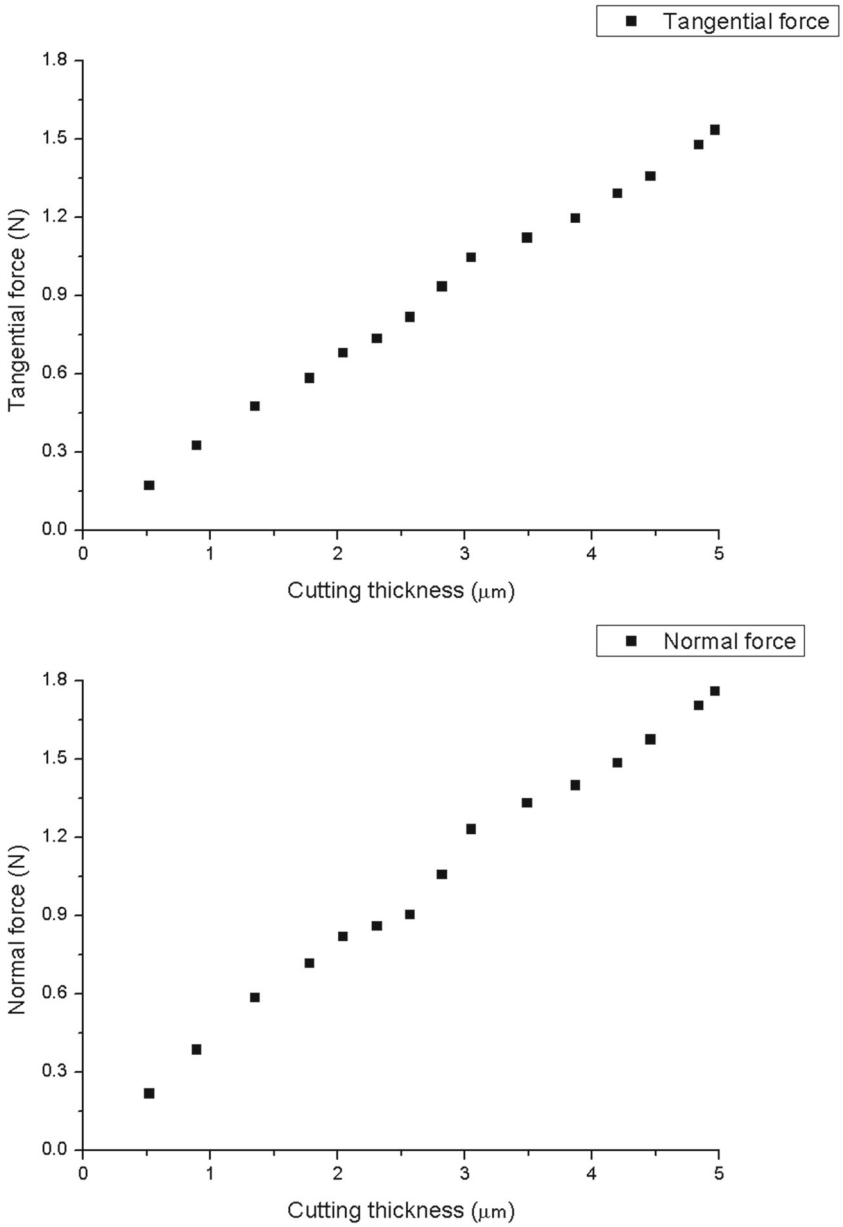

Fig. 4 Resultant forces under different cutting thickness

10 % of error [28]. The general form of the Johnson-Cook dynamic failure model is defined as

$$D = \sum \frac{\Delta \varepsilon_p}{\varepsilon_f} \tag{2}$$

where $\Delta \varepsilon_p$ is the increment of the equivalent plastic strain, ε_f is the failure strain which is defined as

$$\varepsilon_f = [d_1 + d_2 \exp(d_3 \frac{p}{q})][1 + d_4 \ln(\frac{\dot{\varepsilon_p}}{\dot{\varepsilon_0}})][1 + d_5 \frac{T - T_{tran}}{T_{melt} - T_{tran}}] \tag{3}$$

where p is the hydrostatic pressure stress and q is the Mises stress, $\dot{\varepsilon_p}$ and $\dot{\varepsilon_0}$ are the equivalent plastic strain rate and reference strain rates, T is the current temperature, T_{tran} is the transient ambient temperature, T_{melt} is the melting temperature, the failure parameters d1-d5 are summarized by Johnson and Cook [24] and illustrated in Table 2. Other material properties of CBN grit and AI4340 used in this model are illustrated in Table 3.

Additionally, the grinding process settings such as contact definition, grinding parameters and boundary conditions should be considered. It is necessary to define the contact condition between grit and workpiece, especially the frictional relationships in the grinding model. The friction model is given by the Eq. [29]

$$\tau_f = \mu \cdot \sigma_n, \qquad \tau_f < \tau_{max} \tag{4}$$

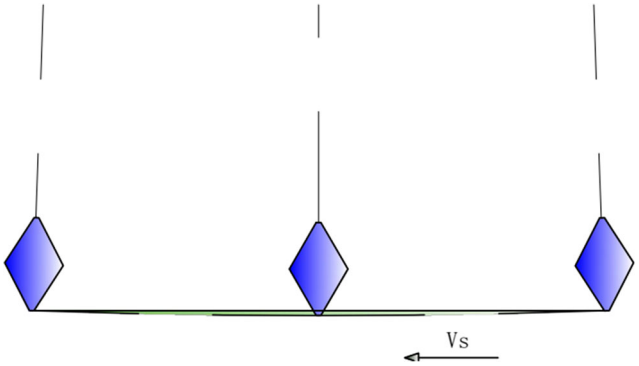

Fig. 5 Actual trajectory of the grit in the simulation

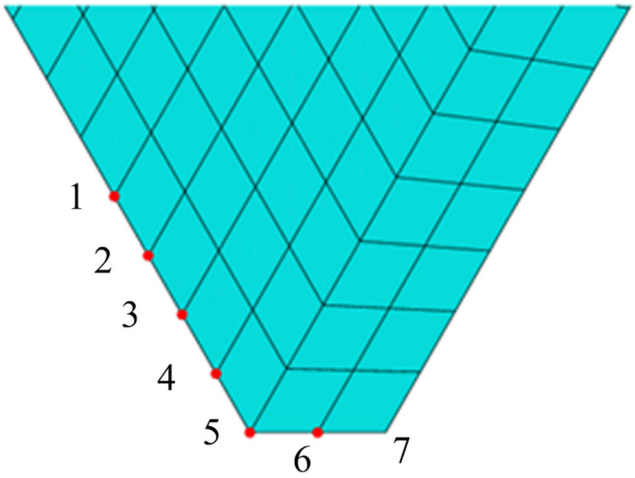

Fig. 7 Critical nodes along the grit surface

$$\tau_f = \tau_{max}, \qquad \tau_f \geq \tau_{max} \tag{5}$$

where τ_f is the frictional stress. σ_n is the normal stress, μ is the Coulomb friction coefficient. The Coulomb friction coefficient is assumed to be 0.24 in this case according to the study by Brocail et al. [30]. The value of the Coulomb friction coefficient was determined by fitting the experimental forces and the numerical ones, similar results were also obtained in the study by Arrazola and Meslin [31]. τ_{max} is the maximum frictional stress and it is usually defined by the Mises criterion in the form of

$$\tau_{max} = \frac{1}{6}[(\sigma_1 - \sigma_2)^2 + (\sigma_2 - \sigma_3)^2 + (\sigma_3 - \sigma_1)^2] = \frac{\sigma_y}{\sqrt{3}} \tag{6}$$

The trajectory of the grit is almost an arc in the case of surface grinding as shown in Fig. 3. The cutting thickness changes during the grinding process, which will lead to different grinding forces. To determine the difference in grinding forces, both tangential and normal force were calculated by scratching the grit on the workpiece. The cutting depth in this calculation was 5 µm and the effective radius was approximately 35,000 µm. The resultant forces under different cutting thickness during single grit grinding are shown in Fig. 4. The grinding forces increased with increasing cutting thickness. The maximum grinding forces occurred when the maximum cutting thickness reached the value of reset cutting depth. It is usually correlated with the maximum un-deformed chip thickness and applied as the load on the vertex of the grit in the research of grit fracture [10, 17]. Considering the radians of the trajectory is very small, as shown in Fig. 5, and the grit fracture evolution is mostly controlled by the maximum grinding forces around the area of maximum cutting depth, the motion of the grit in this simulation is simplified to be linear. This simplification has proven to be appropriate by other researchers for simulating chip formation [6] and calculating the grinding forces [4] in single grit grinding simulations. The grinding speed is approximately 10 m/s, according to the wheel diameter of 70 mm and the rotation speed of 3000 RPM.

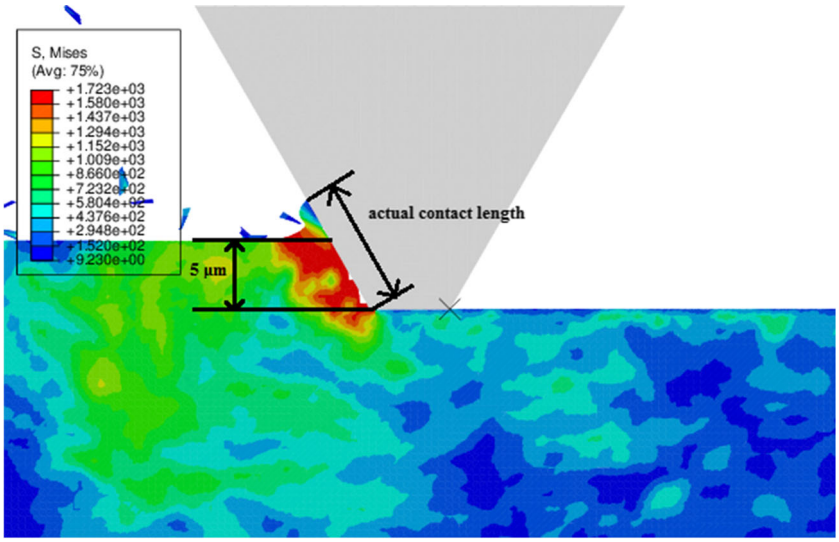

Fig. 6 Single grit grinding simulation

The CBN grit is assumed to be rigid during grinding and the initial temperature of the CBN grit and the workpiece is assumed to be 20 °C. The simulation results of single grit grinding is shown in Fig. 6, the theoretical contact length is approximately 5.88 μm along the rake surface, the actual contact length is approximately 1.5–2 times the length of the theoretical contact length, considering the pile-up and flow of the chip.

As the pile-up height of the grinding chip only reaches the fourth element along the rake surface, the contact forces only exist from node 1 to node 7 along the contact surface as shown in Fig. 7. Considering that the contact force in node 7 is too much smaller than other nodes, the grinding forces were calculated in the six critical nodes from node 1 to node 6 marked in red as shown in Fig. 7. The normal and tangential forces of six critical nodes are shown in Fig. 8a, b. The increment of time is 1×10^{-5} s and the total time is 2×10^{-4} s. The results suggest that the contact forces vary from each node are time dependent. This is primarily because the chip flows along the grit rake surface, which will lead to the consequence of a space and time dependent contact condition. In addition, the chip formed during the single grit grinding process is related to the chip formation mechanism, which will result in fluctuation in the grinding force.

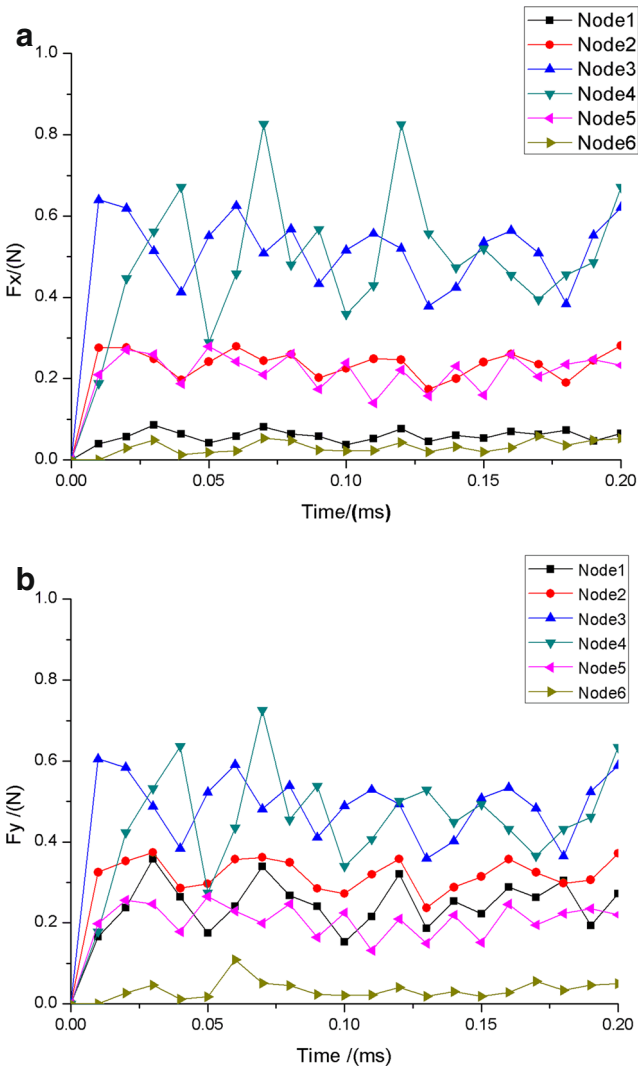

Fig. 8 Grinding forces for critical nodes. **a** Tangential force and **b** normal force

To achieve a more realistic loading state, the normal and tangential force of the six critical nodes will be applied on nodes along the grit vertex instead of a uniform distribution load. The resultant grinding forces are calculated according to the summation of the six critical nodes. The resultant normal and tangential grinding forces are shown in Fig. 9. The average normal force F_n is 1.73 N while the average tangential force F_t is 1.55 N. The ratio of tangential force to normal force is 0.89, which is different from the results obtained by Ding et al. [17]. The reason for this discrepancy is drawn as follows: The grinding force can be decomposed into the tangential force parallel to the X axis and the normal force parallel to the y axis. The tangential force and the normal force are defined by the Eq. [7].

$$F_t = F_{t,c} + F_{t,sl} \tag{7}$$

$$F_n = F_{n,c} + F_{n,sl} \tag{8}$$

where $F_{t,c}$ is the tangential force from cutting and $F_{t,sl}$ is the tangential force from sliding, $F_{n,c}$ is the normal force from cutting and the $F_{n,sl}$ is the normal force from sliding. The ratio of Ft/Fn is controlled by the forces (both tangential and normal) and the ratio of it(in both sliding and cutting area). The ratio of tangential force to normal force is approximately 0.24 (according to the friction coefficient) in the sliding area while the ration is approximately 1.05 (according to the rake angle and friction coefficient of the rake surface) in the cutting area. It is obvious that increasing

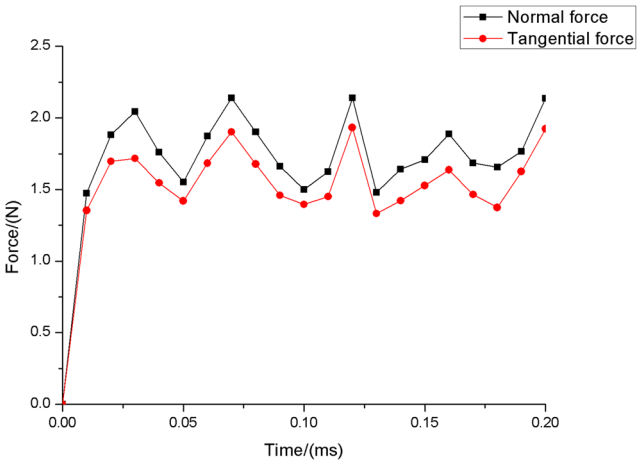

Fig. 9 Normal and tangential grinding force

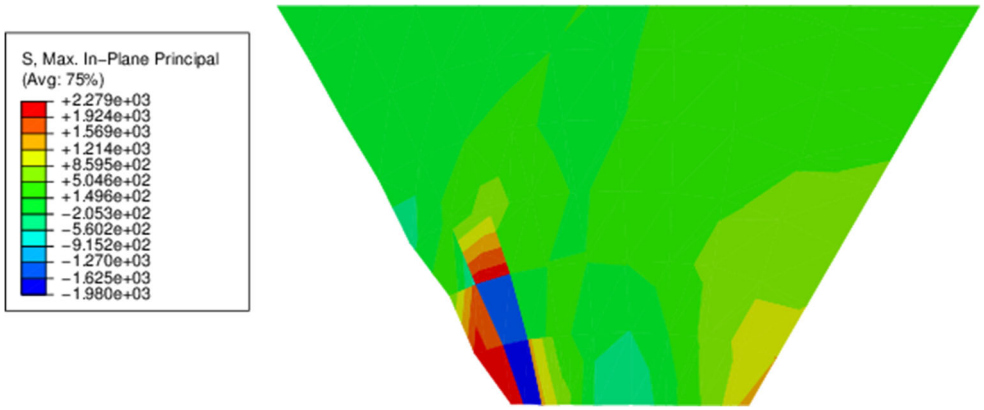

Fig. 10 Stress distribution before fracture

the proportion of the sliding force will decrease the value of the ratio, while increasing the proportion of the cutting force will increase it. The sliding force is the product of the contact length in the flank surface l_1 and the sliding force per unit width $\acute{F_s}l$. The cutting force is the product of the contact length l_2 in the rake surface and the cutting force per unit width $\acute{F_c}$. The sliding forces is generated mostly because of the sliding action and it is dominated by the elastic deformation of the workpiece material in the machined surface. The cutting force is generated by the cutting action and is dominated by the plastic deformation and strain hardening of the un-machined workpiece material. It is suggested that $\acute{F_{sl}}$ is much smaller than $\acute{F_c}$ as the contact pressure between the flank surface and the workpiece is elastic and the depth of interaction is much smaller in the flank surface, while the contact stress reach a maximum at the cutting edge in the rake surface [41]. Therefore, the sliding force is smaller than the cutting force in this simulation as the value of l_1 is 5 µm while the value of l_2 is 5.8 μm. The contact length of the flank surface is much smaller and no blunt radius was assumed in this simulation compared with other cases [4, 8, 17], therefore the force ratio is much larger as a result.

2.3 Finite element model of loading and grit fracture prediction

CBN has a superior level of hardness, second only to diamond, and it is superior to most abrasive materials in thermal-mechanical stability [11]. There are several published works dedicated to investigating the fracture characteristics of CBN, which provides us with a valuable reference respect to the material properties. Pacella et al. studied the wear progress of PCBN micro-abrasive edges and found that abrasive fracture is induced by cracking of the micro-edges results from mechanical and thermal loads [33]. It is suggested by Ichida that the brittle fracture occurs primarily because of the tensile stress although the applied force is compressive [32]. Similar conclusions were obtained by Jackson [10] and Ding [34], they point out that the ratio of compress strength to tensile strength is high in brittle materials, and may rise up to 10:1 in CBN. Zhang et al. investigated the structural deformation and strength of CBN and concluded that the weakest tensile strength is in different orientations, which suggests that the brittle fracture is probably caused by tensile stress although the compressive stress is more prominent [35]. According to the studies mentioned above, some assumptions and simplifications were made before creating the fracture model. (1) Wear due to chemical diffusion and thermal adhesion is ignored, as the CBN grit is relative stable with respect to its chemical-thermal property. (2) Brittle fracture is considered to be caused by the maximum tensile stress. (3) Crystal

Table 4 Coordinates and displacements of boundary nodes

Node	Initial coordinates	Displacements
24	(−54.848, 95)	(0, 0)
295	(−6.5258, 11.3035)	(0.0149, 0.0129)
299	(−3.1009, 5.3713)	(0.0787, 0.0177)
2456	(−2.1116, 5.9221)	(0.0082, 0.0145)
2545	(−1.0314, 6.3235)	(0.0168, 0.0174)
2553	(−0.4569, 4.7098)	(−0.0028, 0.0106)
2561	(0.0613,3.1165)	(0.0101, 0.0104)
2560	(0.94323, 3.2914)	(−0.0020, 0.0114)
2568	(1.2206, 1.6315)	(0.0050, 0.0074)
305	(1.3930, 0)	(−0.0037, 0.0126)
306	(2.1371, 0)	(0.0031, 0.0039)
307	(2.9555, 0)	(0.0009, 0.0173)
308	(3.7911, 0)	(−0.0038, 0.0057)
309	(4.5853, 0)	(−0.0017, 0.0055)
310	(5.33312, 0)	(−0.0026, 0.0025)
19	(5.7738, 0)	(0.0002, 0.0001)
312	(7.1704, 2.4190)	(−0.0021, −0.001)
11	(60.6220, 95)	(0, 0)
25	(8.6605, 185)	(0, 0)
26	(−2.8865, 185)	(0,0)

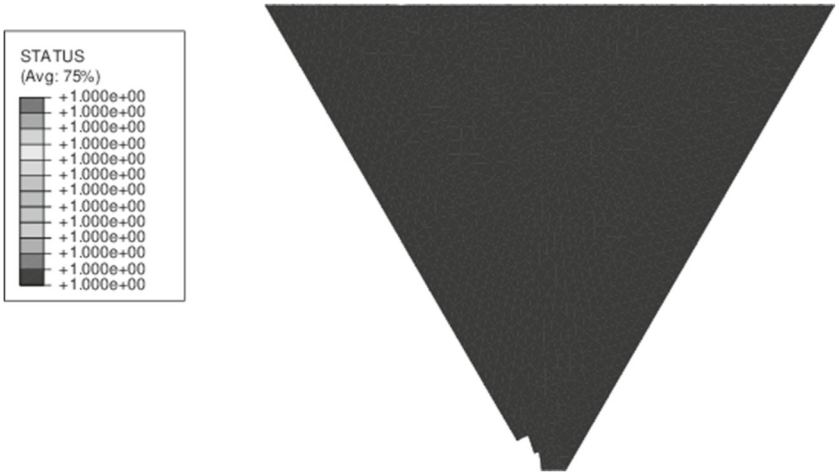

Fig. 11 Geometry of the grit after fracture

defects are neglected. (4) The properties of CBN grit are assumed to be isotropic.

The conventional material properties of CBN are illustrated in Table 3. The brittle cracking model based on the maximum tensile strength criterion is created to simulate the wear evolution of grit fracture. The crack initiation is detected using the Rankine criterion and the maximum tensile stress is set to be 2.34 GPa according to the strength testing experiment conducted by Ichida [32]. The post-failure stress-strain relation is defined by the critical strain energy release rate G_c in order to reduce mesh sensitivities [36]. The value of G_c is determined by the equation

$$G_c = \frac{{K_c}^2}{E} \tag{9}$$

where E is the elastic modulus and equals 710 MPa, and K_c is the stress intensity factor obtained from the experiment conducted by Carolan et al. [37]. The value of K_c is set to be 7.7 MPa.m$^{1/2}$. Thus, G_c is set to be 84 N/m according to Eq. 9. The equivalent grinding forces extracted in the critical nodes in Section 2.2 are applied to the same node along the apex of the grit and the stress distribution in the grit before fracture is obtain as shown in Fig. 10. The maximum tensile stress is almost 2300 MPa in the breaking area while the compressive stress is approximately 4700 MPa. As soon as the element in the contact area is failed, the fracture simulation is terminated to ensure the accuracy of loading.

2.4 Updating grit geometry after fracture

The geometry of the CBN grit is updated in this section according to the wear simulation results. It can be simply divided into three steps to update the geometry: (1) Delete the failed element in the previous fracture prediction model and generates an approximate boundary geometry for the grit. (2) Obtain the original coordinates and deformation displacements of the boundary nodes. (3) Create the

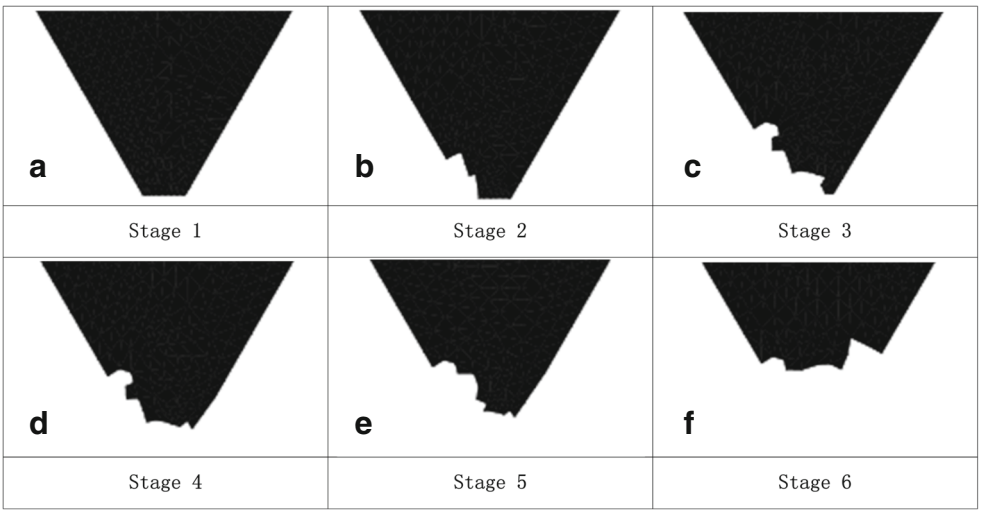

Fig. 12 Grit geometry at various wear stages

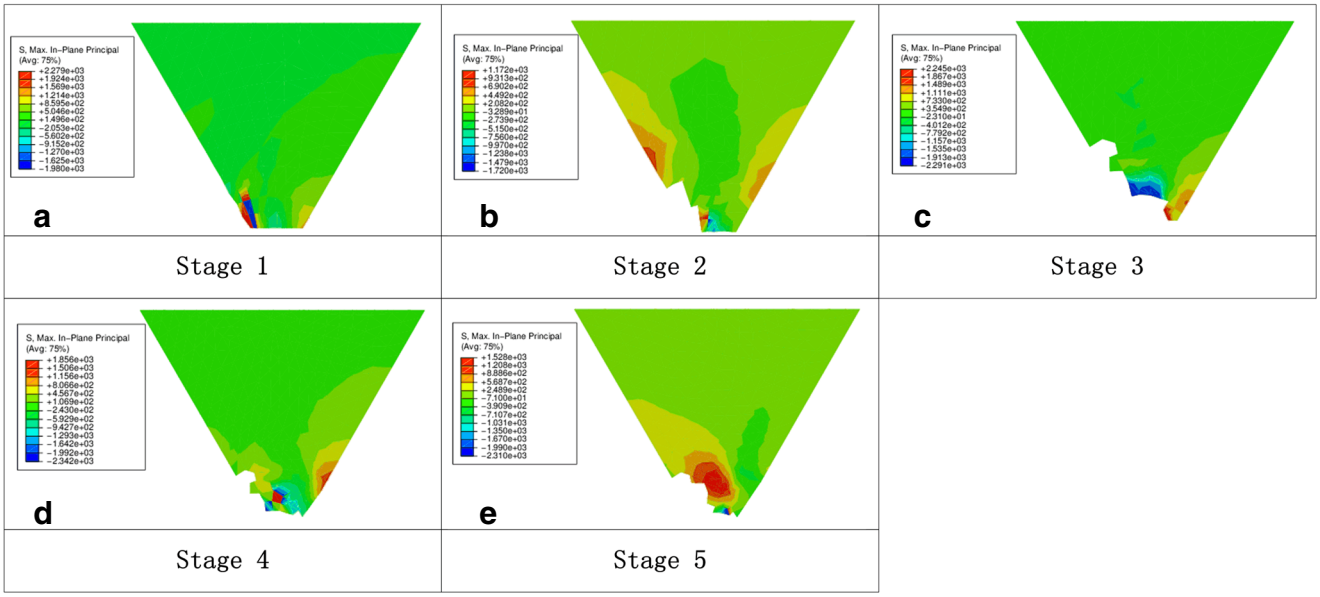

Fig. 13 Contour maps of maximum principle stress at various wear stages

new geometry for the grit according to the coordinates of the boundary nodes after deformation. There are 10 failed elements on the vertex of the grit and then the approximate boundary shape of the grit is obtained. The nodes on the boundary were extracted and the coordinates and displacements are illustrated in Table 4. The updated geometry of the CBN grit after fracture is generated according to the deformed coordinates by summation of the initial coordinates and displacements, as illustrated in Fig. 11.

3 Results and discussion

3.1 Grit geometry and stress distribution at various wear stages

The simulation procedure illustrated in Fig. 1 was repeated five times until the grit lost contact with the workpiece. Six wear stages are presented according to the updated grit geometry, shown in Fig. 12. The contour maps of the

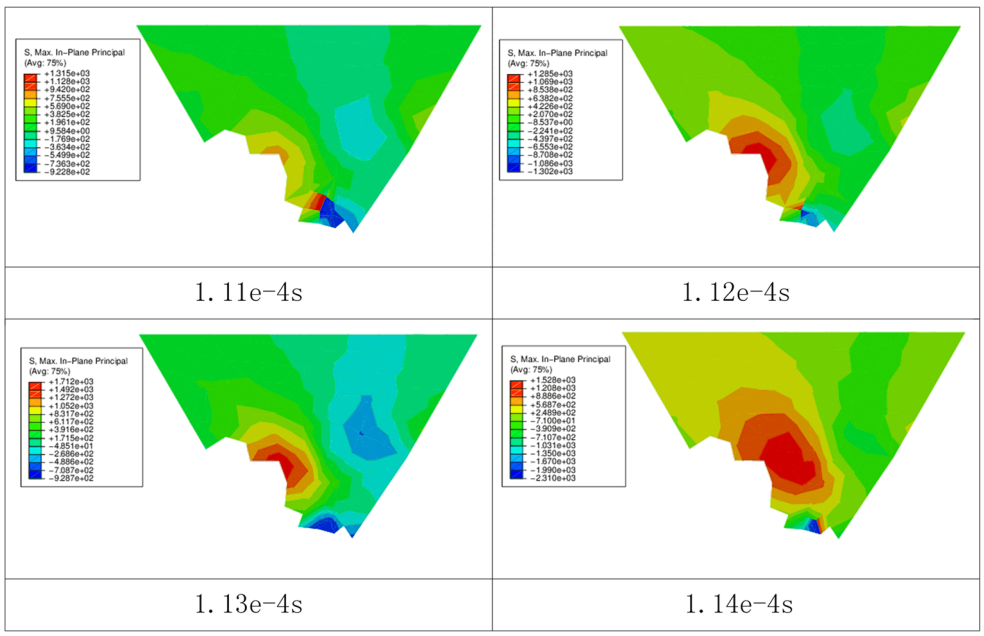

Fig. 14 Evolution of stress distribution at various grinding times at stage 5

maximum principle stress at various wear stages are shown in Fig. 13. At stage 1, the grit is assumed to be intact. The grinding process was dominated by the cutting edge whose rake angle is −30° and the width of the flank surface is 5 μm. The grinding distance is 730 μm. The stress distribution before fracture is shown in Fig. 13a, where the maximum principle stress is mostly concentrated in the rake surface of the grit approaching to the vertex. In addition, it also occurs in a relatively smaller area inside the grit. The maximum tensile principle stress is 2280 MPa. The resultant geometry at stage 2 is shown in Fig. 12b, where the rake surface of the grit is fractured and two main cutting edges are generated. The rake angle of the first cutting edge is approximately −17° and the flank angle is 10°. The rake angle of the second cutting edge is −8° while the flank angle is approximately 2° because of the deformation caused by scratching. The grinding distance is 920 μm. The maximum principle stress distribution before fracture is shown in Fig. 13b, the tensile stress concentration occurs approaching the second cutting edge inside the grit. At stage 3, the geometry of the worn grit is shown in Fig. 12c, which is more complicated with multiple cutting edges along the rake face. Theses micro-cutting edges have both negative and positive rake angles. The flank surface of the grit is almost worn and only a thin cutting edge is left. The grinding distance is 380 μm. The maximum principle stress occurs in the rake surface of this cutting edge as shown in Fig. 13c, and the value of it is approximately 2245 MPa. The thin cutting edges formed at the previous stage are fractured due to the maximum tensile stress and a new bottom surface is generated at stage 4, as shown in Fig. 12d. This newly generated bottom surface can be considered the new flank surface of the grit and the maximum protrusion height of the grit decreases by 2.3 μm. The rake surface of the worn grit is relatively intact, and only slight deformation occurs. The grinding distance is 610 μm. The stress distribution before fracture is shown in Fig. 13d, where the maximum tensile principle stress mostly occurs inside the grit approaching the rake surface. The concentrated tensile stress causes grit wear in the rake surface, and new cutting edges are generated in stage 4, as shown in Fig. 12e. There are two main cutting edges formed in this stage whose rake angle are positive. The rake angle of the first cutting edge is approximately 6.5°, while that of the second cutting edge is approximately 22.5°. The grinding distance is 1150 μm. The maximum principle stress distribution before fracture wear at this stage is shown in Fig. 13e. The area of the concentrated stress is relatively larger and the evolution of stress distribution before fracture with increasing grinding time is illustrated in Fig. 14. The concentrated tensile stress is diffused from the singularity along the rake surface of the grit, which results in a large amount of material removal in the contacting area. The maximum principle tensile stress increased from 940 MPa to 1670 MPa and the worn geometry after fracture is shown in Fig. 12f. A new bottom surface is formed at stage 6 and this result is similar to the resultant geometry at stage 3. However, the volume of grit material removal is larger at stage 5 in comparison. It is because the cutting edge formed in the bottom surface at stage 3 is thin and easy to fracture, which prevents further grit fracture from occurring. The maximum protrusion height of the grit at stage 6 decreases by 8.5 μm. The grit is considered to wear out as the initial grinding depth is set to be 5 μm and the grit is unable to interact with the workpiece.

3.2 Grinding forces at various wear stages

The grinding forces induced by the grit at various wear stages are illustrated in Fig. 15, including the normal force

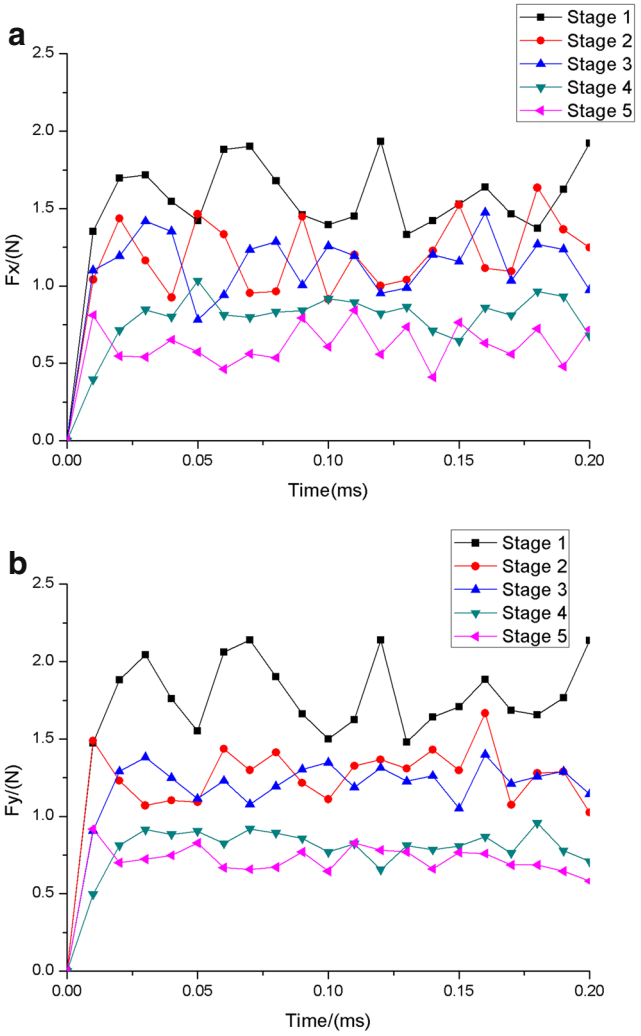

Fig. 15 Grinding forces at various wear stages. **a** Tangential force and **b** normal force

and tangential force. The results suggest that both the normal and tangential force are time-dependent. The maximum grinding force is approximately 1.4–2 times the size of the minimum grinding force. For example, the maximum normal force at stage 1 is 2.14 N while the minimum normal force is 1.47 N. As is shown by several researchers, the grinding process can be divided into three phases, named rubbing, ploughing and cutting [38]. The grinding force differs between the three phases and it is widely accepted that the rubbing force is caused by elastic interaction and is less than the ploughing force caused by both elastic deformation and plastic upheaval [23]. This occurs primarily because the grinding phase transition results in fluctuation in the normal grinding force, which can be seen in the experimental results obtained by Azizi and Mohamadyari through single grit scratching test [39]. On the other hand, the grinding force usually decreases when chips are formed, which suggests the maximum grinding force occurs at the transition point between ploughing and cutting phases. The reason for this phenomenon is that when the ploughed material is removed in the form of chips the ploughing upheaval decreases, and which results in a reduction of ploughing force. Similar conclusions were obtained in the turning process, and it is suggested that the release of cutting energy accumulated ahead of the cutting edge in a short time is the main reason for the transient decrease in the cutting force [40].

Additionally, the grinding force varies at different stages. It is inevitable as the geometry of girt changes because of fracture wear. To compare the forces, the average grinding forces at various stages were calculated. Thus, the influence of grinding force fluctuation caused by phase transition is reduced, and the results are shown in Fig. 16. The grinding force decreases rapidly from stage 1 to stage 2. This occurs mostly because the number of cutting edges increases in the rake surface of grit at stage 2 and the bottom surface of the grit is smaller, which can reduce the scratching effect in the flank surface. The grinding force at stage 3 is also smaller than at stage 2 with the number of cutting edges increased. It seems like the grinding force decreases at stage 4 and stage 5. However, the maximum cutting depth decrease by approximate 50 % at stage 4 and stage 5. To make an appropriate comparison, the equivalent grinding force is calculated using the ratio of grinding force to the maximum cutting depth. The result is shown in Fig. 17, which suggests an increase in the equivalent grinding force from stage 3 to stage 4. It is because the sharp cutting edge in the bottom surface of the grit are fractured and a new flank surface is formed in stage 4, which can be considered a dulling process. However, it decreases afterward, primarily because both the rake surface and flank surface is fractured at stage 5, which generates new micro-cutting edges in the rake surface. This phenomenon can be considered a self-sharpening process.

3.3 Material removal at various stages

Figure 18 shows the material removal process at various wear stages. It can be seen that only one cutting edge is working at stage 1, while two main cutting edges are working at stage 2. It can be found the material pile-up height is relatively high at stage 1, as the material upheaval is blocked at stage 2. The piled-up material is more likely to be cut off and collapses into fragmented chips under the pressure of fractured flank surface at this stage. Thus, the grinding forces at stage 2 are much smaller than at stage 1. The material removal process at stage 3 is similar to that at stage 1. With increasing fracture of the rake surface, the piled-up material is able to flow along the fractured surface. Although the width of the flank surface at stage 4 (6.3 μm) is larger than that at stage 1 (5 μm), the real contact width of the flank surface is much smaller. This occurs mostly because the geometry of the flank surface at this stage is irregular, which

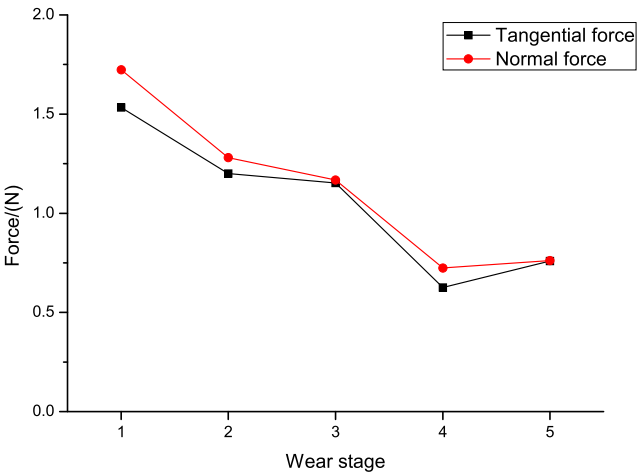

Fig. 16 Average grinding force at various wear stags

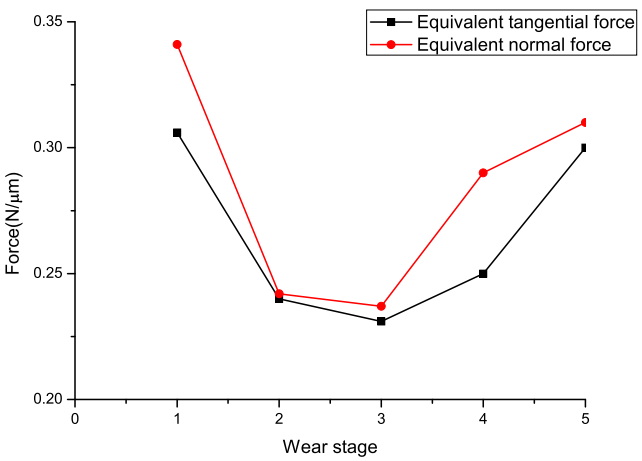

Fig. 17 Equivalent average grinding force at various wear stages

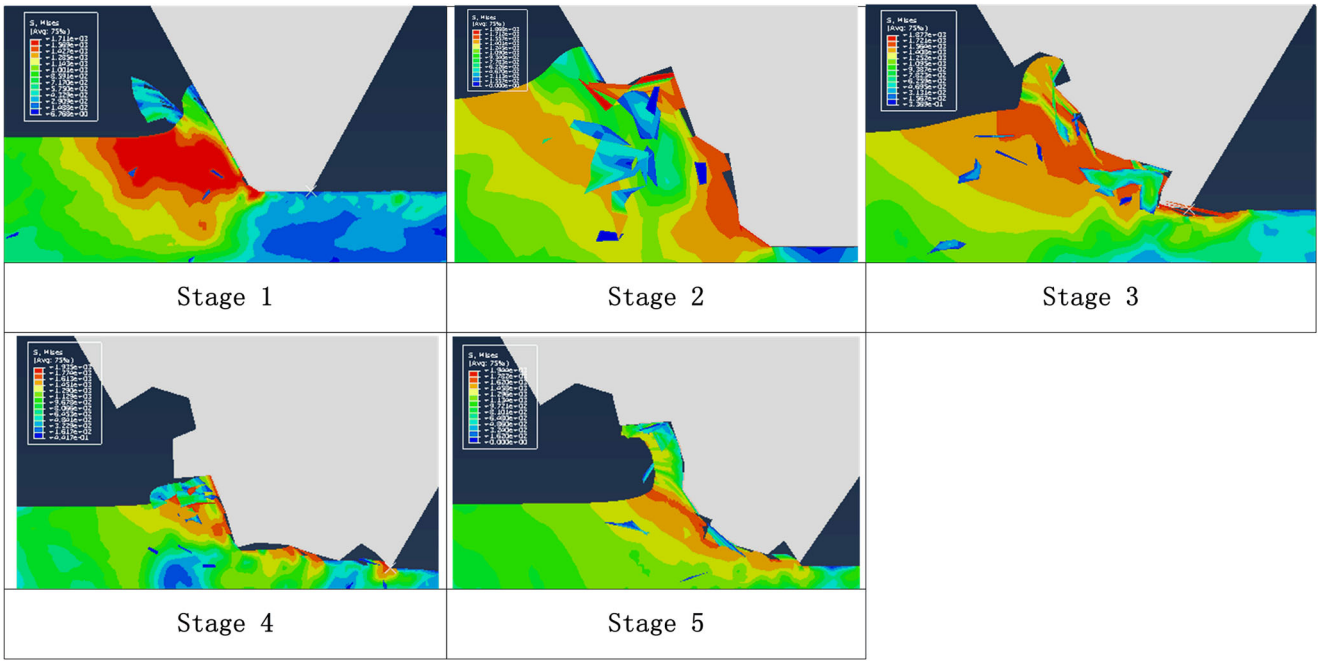

Fig. 18 Material removal at various wear stages

results in multiple-points contact in some area. The pile-up of the material was also blocked at stage 4; therefore, the geometry of the chip is stochastic and irregular. The cutting behavior at stage 5 is different from the other stages as the rake angle of the main cutting edges at this stage is positive. The positive rake cutting edge results in continuous chip formation at this stage. The cutting efficiency is relatively high; however, concentrated stress is more likely to occur at this stage. As a consequence, the fracture effect is more sever at this stage. The volume of the grinding chip is analyzed using the distorted elements removed during the simulation. It is found that the volume decreases as the number of cutting edges increases, which may result from a decrease in the cutting depth of each cutting edge.

4 Conclusions

A new methodology for single grit cutting simulation was presented in this paper, which considered the fracture effects of the grit. The wear evolution and its impact on cutting performance was studied by recycling the simulation procedure based on the FE method. The main conclusions of this research can be drawn as follows:

1. The grit fracture is primarily caused by the maximum tensile stress. The fracture may result in a self-sharpening effect or a dulling effect at different wear stages. The maximum tensile stress reaches approximately 2300 MPa and it usually occurs along the rake surface of the cutting edges. The wear process was found to be an interweaving and alternating process consisted of dulling and shelf-sharpening.
2. The grinding force varies at different wear stages. The number of the cutting edges is important to the resultant force. Both the tangential and normal force tends to decrease with an increase in the cutting edge' number. The geometry of micro-cutting edges is complicated after the grit fracture. The grit may cut with both positive and negative rake angle cutting edges. The real contact area of the grit flank surface is important to the resultant normal grinding force, as the scratching effect increases with larger sliding area. The grinding phases transition will also influence the grinding force and result in fluctuation in both normal and tangential grinding forces. The maximum grinding force may occur at the transition point between the ploughing and cutting phase as the chip formation energy is released in a transient time.
3. The material removal also varies at different wear stages. The pile-up height is controlled by both the rake surface and the flank surface. Although the fractured flank surface does not participate in the cutting process directly, chips are more easily formed under extrusion. The volume of the grit chip is relatively small when worn grit with multiple cutting edges is working. This occurs primarily because the real cutting depth decreases as the workpiece material is removed under the joint action by these micro-cutting edges.

Acknowledgments The authors would like to thank the National Nature and Science foundation of China (Grant No. 71071138).

References

1. Butler-Smith PW, Axinte DA, Daine M (2009) Preferentially oriented diamond micro-arrays: a laser patterning technique and preliminary evaluation of their cutting forces and wear characteristics. Int J Mach Tools Manuf 49:1175–1184
2. Axinte D, Butler-Smith PW, Akgun C, Kolluru K (2013) On the influence of single grit micro-geometry on grinding behavior of ductile and brittle materials. Int J Mach Tools Manuf 74:12–18
3. Anderson D, Warkentin A, Bauer R (2011) Experimental and numerical investigations of single abrasive-grain cutting. Int J Mach Tools Manuf 51:898–910
4. Anderson D, Warkentin A, Bauer R (2012) Comparison of spherical and truncated cone geometries for single abarasive-grain cutting. J Mater Process Technol 212:1946–1953
5. Tahsin TÖ, Chen X (2012) Experimental investigation of material removal mechanism in single grit grinding. Int J Mach Tools Manuf 63:32–40
6. Ohbuchi Y, Obikawa T (2005) Adiabatic shear in chip formation with negative rake angle. Int J Mech Sci 47:1377–1392
7. Malkin S, Cook NH (1971) The wear of grinding wheels: Prat 1-Attritios wear. J Eng Ind 93:1120–1128
8. Wu HY, Huang H, Jiang F, Xu XP (2016) Mechanical wear of different crystallographic orientations for single abrasive diamond scratching on Ta12W. Int J Ref Metals Hard Mater 54:160–269
9. Shi Z, Malkin S (2006) Wear of electroplated CBN grinding wheels. J Manuf Sci Eng 128:110–118
10. Jackson MJ (2007) Modeling of fracture wear in vitrified cBN grinding wheels. J Achiev Mater Manuf Eng 24:230–236
11. Fujimoto M, Ichida Y (2008) Micro fracture behavior of cutting edges in grinding using single crystal cBN grains. Diamond Relat Mater 17:1759–1763
12. Ding WF, Xu JH, Chen ZZ, Su HH, Fu YC (2010) Grain wear of brazed polycrystalline CBN abrasive tools during constant-force grinding TiC6AlC4V alloy. Int J Adv Manuf Technol 52:969–976
13. Miao Q, Ding WF, Xu JH, Yang Y, Fu YC (2013) Fractal analysis of wear topography of brazed polycrystalline cBN abrasive grains during grinding nickel super alloy. Int J Adv Manuf Technol 68:2229–2236
14. Guo G, Shi Z, Atiia H, Mclntosh D (2007) Power and wheel wear for grinding nickel alloy with plated CBN wheels. Ann CIRP 56:343–346
15. ABainia S, Ouelaa N (2015) Experimental study of the combined influence of the tool geometry parameters on the cutting forces and tool vibrations. Int J Adv Manuf Technol 79:1127–1138
16. Farhat ZF (2003) Wear mechanism of CBN cutting tool during high-speed machining of mold steel. Mater Sci Eng A361:100–110
17. Ding WF, Zhu YJ, Xu JH, Fu YC (2015) Finite element investigation on the evolution of wear and stresses in brazed CBN grits during grinding. Int J Adv Manuf Technol 81:985–993
18. Attanasio A, Ceretti E, RIzzuti S, Umbrello D, Micari F (2008) 3D finite element analysis of tool wear in machining. CIRP Ann Manuf Technol 57:61–64
19. Arrazola PJ, Ozel T, Umrello D, Davies M, Jawahir IS (2013) Recent advances in modelling of metal machining processes. CIRP Ann Manuf Technol 62:695–718
20. Zhu YJ, Ding WF, Xu JH, Fu YC (2014) Surface fractal evolution of fracture behavior of polycrystalline cBN grains in high-speed grinding. Int J Adv Manuf Technol 76:1505–1513
21. Suh CM, Bae KS, Suh MS (2009) Wear behavior of diamond wheel for grinding optical connector ferrule FEA and wear test. J Mech Sci Technol 22:2009–2015
22. Akbari M, Buhl S, Leinenbach C, Spolenak R, Wegener K (2012) Thermomechanical analysis of residual stresses in brazed diamond metal joints using Raman spectroscopy and finite element simulation. Mech Mater 52:69–77
23. Doman DA, Warkentin A, Bauer R (2009) Finite element modeling approaches in grinding. Int J Mach Tools Manuf 49:109–116
24. Johnson GR, Cook WH (1983) A constitutive model and data for metals subjected to large strains, high strain rates and high temperatures. Proc 7th Int Symp Ballist 21:541–547
25. Guo YB, Yen DW (2004) A FEM study on mechanisms of discontinuous chip formation in hard machining. J Mater Process Technol 155–156:1350–1356
26. Ozel T, Karpat Y (2008) Hard turning with variable microgeometry PcBN tools. Ann CIRP 57:73–76
27. Johnson GR, Cook WH (1985) Fracture characteristics of three metals subjected to various strains, strain rates, temperatures and pressures. Eng Fract Mech 21:31–48
28. Zhang YC, Mabrouki T, Nelias D, Gong YD (2011) Chip formation in orthogonal cutting considering interface limiting shear. Finite Elements Anal Des 47:850–863
29. Zorev NN (1963) Inter-relationship between shear processes occurring along tool face and shear plane in metal cutting. Int Res Product Eng:49
30. Brocail J, Watremez M, Dubar L (2010) Identification of a friction model for modelling of orthogonal cutting. Int J Mach Tools Manuf 50:807–814
31. Arrazola P, Meslin F (2003) A technique for the identification of friction at tool/chip interface during machining. In: Proceedings 6th CIRP international workshop on modeling of machining operations
32. Ichida Y (2008) Mechanical properties and grinding performance of ultrafine-crystalline cBN abrasive grains. Diamond Relat Mater 17:1791–1795
33. Pacella M, Axinte DA, Butler-Smith PW, Shipway P, Daine M, Wort C (2015) An assessment of the wear characteristics of microcutting arrays produced from polycrystalline diamond and cubic boron nitride composites. J Manuf Sci Eng 138:021001-1,021001-15
34. Ding WF, Xu JH, Chen ZZ, Su HH, Fu YC (2010) Wear behavior and mechanism of single-layer brazed CBN abrasive wheels during creep-feed grinding cast nickel-based superalloy. Int J Adv Manuf Technol 51:541–550
35. Zhang Y, Sun H, Chen CF (2006) Structural deformation,strength,and instability of cubic BN compared to diamond. Phys Rev:73
36. Hillerborg A, Modeer M, Peterson PE (1976) Analysis of crack formation and crack growth in concrete by means of fracture mechanics and finite elements. Cement Concrete Res 6:773–781
37. Carolan D, Alveen P, Ivankovic A, Murphy N (2011) Effect of notch root radius on fracture toughness of polycrystalline cubic boron nitride. Eng Fract Mech 78:2885–2895
38. Hahn RS (1962) On the nature of the grinding process. In: Proceedings of the 3rd machine tool design and research conference, pp 129–154
39. Azizi A, Mohamadyari M (2015) Modeling and analysis of grinding forces based on the single grit scratch. Int J Adv Manuf Technol 78:1223–1231
40. Neslusan M, Micieta B, Micieovta A, Cillikova M, Mrkvica I (2015) Detection of tool breakage during hard turning through acoustic emission at low removal rates. Measurement 70:1–13
41. Zorev NN (1966) Mechanics of contact on clearance surface. Metal Cutting Mechanics. Pergamon Press Chap.3:129–180